J. metamorphic Geol., 2005, **23,** 1–17 doi:10.1111/j.1525-1314.2005.00554.x

Phase relationships in grunerite–garnet-bearing amphibolites in the system CFMASH, with applications to metamorphic rocks from the Central Zone of the Limpopo Belt, South Africa

A. ZEH[1], T. J. B. HOLLAND[2] & R. KLEMD[1,3]
[1]*Mineralogisches Institut, Universität Würzburg, Am Hubland, D-97074 Würzburg, Germany (armin.zeh@mail.uni-wuerzburg.de)*
[2]*Department of Earth Sciences, University of Cambridge, Cambridge CB2 3EQ, UK*
[3]*Rand Afrikaans University, Geology Department, Johannesburg, South Africa*

ABSTRACT A petrogenetic grid in the model system CaO–FeO–MgO–Al_2O_3–SiO_2–H_2O is presented, illustrating the phase relationships among the minerals grunerite, hornblende, garnet, clinopyroxene, chlorite, olivine, anorthite, zoisite and aluminosilicates, with quartz and H_2O in excess. The grid was calculated with the computer software THERMOCALC, using an upgraded version of the internally consistent thermodynamic dataset HP98 and non-ideal mixing activity models for all solid solutions. From this grid, quantitative phase diagrams (*P–T* pseudosections) are derived and employed to infer a *P–T* path for grunerite–garnet-bearing amphibolites from the Endora Klippe, part of the Venetia Klippen Complex within the Central Zone of the Limpopo Belt. Agreement between calculated and observed mineral assemblages and garnet zonation indicates that this part of the Central Zone underwent a prograde temperature and pressure increase from *c.* 540 °C/4.5 kbar to 650 °C/6.5 kbar, followed by a post-peak metamorphic pressure decrease. The inferred *P–T* path supports a geotectonic model suggesting that the area surrounding the Venetia kimberlite pipes represents the amphibolite-facies roof zone of migmatitic gneisses and granulites that occur widely within the Central Zone. In addition, the *P–T* path conforms to an interpretation that the Proterozoic evolution of the Central Zone was controlled by horizontal tectonics, causing stacking and differential heating at *c.* 2.0 Ga.

Key words: THERMOCALC; CFMASH; grunerite; Limpopo Belt; petrogenetic grid.

INTRODUCTION

Amphiboles of the grunerite–cummingtonite solid-solution occur in a wide range of lithologies together with quartz, chlorite, hornblende, garnet, plagioclase, clinopyroxene, orthopyroxene, olivine, siderite, ankerite, magnetite, hematite and ilmenite. Assemblages among these minerals are observed in medium to high-grade metamorphic rocks, comprising banded iron formations (e.g. Klein, 1966; Immega & Klein, 1976; Gole & Klein, 1981; Miyano & Klein, 1986), alkali-poor amphibolites (e.g. Hoinkes & Mogessi, 1986; Hollocher, 1991; Mottana *et al.*, 1994) and quartzo-feldspathic rocks (Kenah & Hollister, 1983).

The phase relationships and stability field of grunerite–cummingtonite-bearing assemblages have been investigated by experimental studies (e.g. Fonarev *et al.*, 1977, 1979; Fonarev & Korolkov, 1980; Lattard & Evans, 1992), field studies in combination with conventional thermobarometry on adjacent rocks (e.g. Immega & Klein, 1976; Hoinkes & Mogessi, 1986; Hollocher, 1991) and theoretical calculations based on internally consistent thermodynamic datasets. So far, the theoretical studies are focused on phase relationships in the model systems FeO–MgO–SiO_2–H_2O–CO_2–O (FMSHCO; Miyano & Klein, 1986) and FMSH(O) (Miyano & Klein, 1983; Evans & Ghiorso, 1995), which were employed to explain grunerite–cummingtonite assemblages in banded iron formations with orthopyroxene, olivine, quartz and magnetite/hematite and/or siderite. However, because of the system restrictions these models are unable to explain mineral assemblages comprising aluminium- and calcium-bearing minerals such as garnet, clinopyroxene, hornblende, chlorite and plagioclase, which may occur in meta-amphibolites (e.g. Hoinkes & Mogessi, 1986).

In order to close this gap, we present a new petrogenetic grid in the model system CaO–FeO–MgO–Al_2O_3–SiO_2–H_2O (CFMASH). This grid and related phase diagrams like *P–T* pseudosections, *T–X* sections and compatibility diagrams are calculated with an upgraded version of the computer software THERMOCALC version 3.1, using a modification of the internally consistent thermodynamic dataset of Holland & Powell (1998) and activity models presented in the Appendix. Finally, in order to test whether the results of the theoretical calculations are suitable to explain

natural mineral assemblages, quantitative phase diagrams (P–T pseudosections) are applied to better understand the evolution of grunerite-bearing rocks collected from the Endora Klippe situated north of the Venetia kimberlite pipes within the Central Zone of the Limpopo Belt. The derived P–T path provides a new constraint on the geotectonic interpretation of the Limpopo Belt, and the geological significance of this constraint is discussed. Mineral abbreviations follow Kretz (1983).

PHASE DIAGRAMS

Petrogenetic grid

The CFMASH petrogenetic grid is calculated for medium to high-grade metamorphic rocks within a temperature–pressure range of 480–750 °C and 2–12 kbar with quartz and H_2O in excess. Non-ideal solid solutions are used for the minerals grunerite, hornblende, chlorite, garnet, clinopyroxene, and the end-member minerals anorthite, zoisite, kyanite, sillimanite and andalusite. In addition, the subsystems CaO–FeO–Al_2O_3–SiO_2–H_2O (CFASH) and FMSH consider margarite and orthopyroxene, respectively. Activity models used for the solid solutions are given in the Appendix.

The subsystems CFASH and CMASH

As a preliminary step, phase relationships in the subsystems CFASH and CaO–MgO–Al_2O_3–SiO_2–H_2O (CMASH) were investigated (Fig. 1). All stable invariant points in these systems are listed in Table 1. The petrogenetic grid in Fig. 1a shows that grunerite in the system CFASH is stable in a temperature range between 500 and 650 °C. It also demonstrates that grunerite–anorthite assemblages are restricted to pressures <3–4 kbar, while assemblages with garnet + hornblende occur at pressures >3–4 kbar. Additionally, the diagram shows that grunerite–olivine assemblages in CFASH are stable only in a very narrow stability field, which is bracketed by the FSH reaction (Gru = Fa) and the CFASH reactions (Gru = Grt + Cpx + Ol, Gru = Grt + Ol + Hbl and Gru = An + Ol + Hbl). Clinopyroxene–grunerite assemblages require temperatures in excess of 540 °C, whereas chlorite will disappear via the FASH reaction (Chl = Alm + Gru) at temperatures >540 °C and hornblende is stable until around 610 °C. Furthermore, two singularity points occur along the reaction between Grt, Zo, Cpx, An, and are caused by the widely varying garnet composition.

In the CMASH system the assemblage cummingtonite–anorthite is stable from 560 °C/2 kbar to 750 °C/10 kbar, and hornblende within the whole range of the P–T diagram (Fig. 1b, inset). In contrast to the CFASH system, garnet and olivine are absent in the CMASH system.

The system CFMASH

In the system CFMASH, three invariant points are stable in the considered P–T range (Table 1). The univariant reactions emanate or terminate at the CFASH or CMASH subsystem invariant points, except for the reaction that connects the CFMASH invariant points (Fig. 1b). Grunerite–cummingtonite solid-solutions (Gru_{ss}) are stabilised initially by the reactions Chl + Grt + Hbl = Gru + An (at pressures between 2.7 and 8 kbar) and Grt + Hbl + Chl = Gru + Ky (at pressures above 8 kbar). Similar to the CFASH diagram, olivine–Gru_{ss}–anorthite assemblages are stable at pressures below 3–4 kbar, together with garnet, hornblende or clinopyroxene (Fig. 1b). In the absence of anorthite the olivine–Gru_{ss} stability field extends to much higher pressures, where these minerals form assemblages either with garnet or hornblende. The clinopyroxene–Gru_{ss}–anorthite assemblage is restricted to pressures below 4.5 kbar at temperatures above 710 °C, but may extend to higher pressures in the absence of anorthite.

Compatibility diagrams and *T–X* sections

In addition to the petrogenetic grid, phase relationships between the minerals considered are presented in a series of compatibility diagrams (Fig. 2), using a projection from anorthite, quartz and H_2O (all in excess) onto the projection plane of zoisite ($Ca_4Al_6O_{13}$), almandine ($Fe_3Al_2O_6$) and pyrope ($Fe_3Al_2O_6$). As the aluminosilicates (kyanite, sillimanite and andalusite) plot above the projection plane, their phase relationships can only be shown schematically. Furthermore, two T–X_{Fe} sections at 3.5 and 4.5 kbar with anorthite, quartz and H_2O in excess and for a specific rock composition with respect to $CaO/(CaO + Al_2O_3)$ are presented in Fig. 3. The compatibility diagrams and T–X sections illustrate that olivine in the CFMASH system is only stable in very Fe-rich rocks at low pressure conditions, whereas Gru_{ss} can occur in many different assemblages, comprising rocks with low to intermediate Al and Ca contents, and variable Fe/(Fe + Mg) ratios. Garnet has the widest stability range, and occurs in many assemblages in Fe and/or Ca-rich rocks, although not in Mg-rich lithologies. Clinopyroxene assemblages are generally restricted to low-Al, Ca-rich lithologies.

APPLICATION TO NATURAL ROCKS

Generalities

The petrogenetic grid in Fig. 1b considers monoclinic grunerite–cummingtonite solid solutions but no orthoamphiboles such as anthophyllite and gedrite, which will occur during the transformation of Gru_{ss} in Mg-rich lithologies (see Hollocher, 1991; Evans & Ghiorso, 1995). Thus, the grid may only be applied to rocks with high to intermediate Fe/(Fe + Mg)

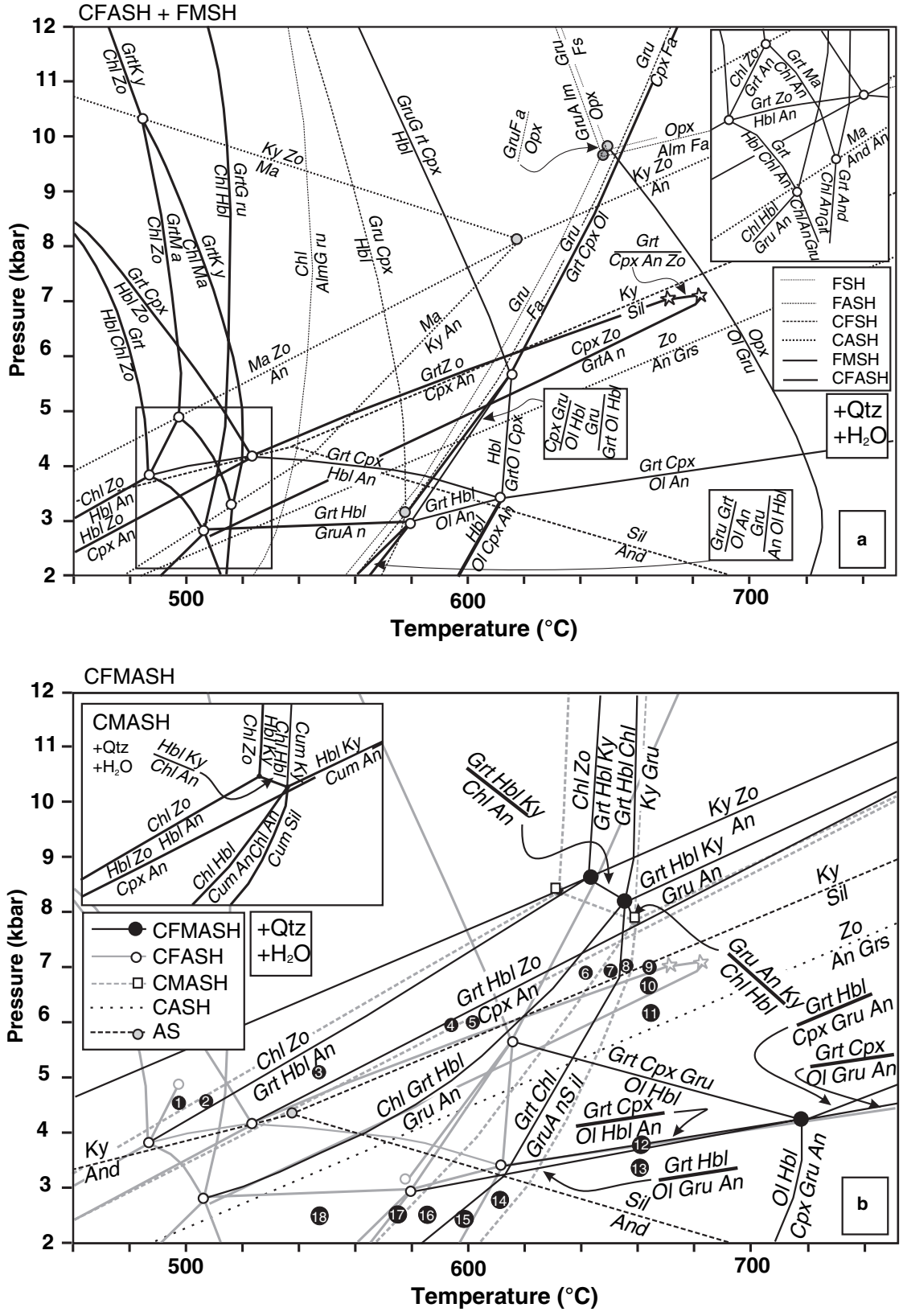

Fig. 1. Petrogenetic grids showing phase relationships in the system CFASH and FMSH (a), CFMASH (b) and CMASH (b, inset). The numbers (1–18) are related to the compatibility diagrams shown in Fig. 2.

Table 1. Invariant points in the system CFASH, CMASH and CFMASH, related to the phase diagrams shown in Fig. 1, and compositional parameters as explained in the Appendix.

Phases	*P* (kbar)	*T* (°C)	Ca(Grt)	*y*(Hbl)	Ca(Hbl)	*y*(Chl)	Q(Chl)	*y*(Gru)	ca(Gru)	ct(Cpx)	fs(Cpx)	Ca(Ol)
Invariant assemblages in CFASH (+Qtz + H_2O)												
Grt, Hbl, Chl, An, Zo	3.83	487.7	0.3770	0.2110	0.9955	0.5259	0.4735					
Grt, Chl, An, Ma, Zo	4.84	497.6	0.2514			0.6314	0.3685					
Grt, Chl, Ky, Ma, Zo	10.41	483.3	0.2145			0.7777	0.2223					
Grt, Hbl, Gru, Chl, An	2.86	506.8	0.2491	0.2061	0.9899	0.5250	0.4742	0.00841	0.01659			
Grt, Chl, And, An, Ma	3.22	517.3	0.09331			0.8225	0.1775					
Grt, Cpx, Hbl, An, Zo	4.14	523.9	0.4995	0.1650	0.9958					0.01101	0.00099	
Grt, Ol, Hbl, Gru, An	2.94	580.3	0.2604	0.1630	0.9815			0.00953	0.02587			0.00085
Grt, Ol, Cpx, Hbl, An	3.32	615.9	0.2976	0.1492	0.9807					0.01212	0.00445	0.00147
Grt, Ol, Cpx, Hbl, Gru	5.735	618.41	0.2676	0.1018	0.9723			0.00726	0.03369	0.00744	0.00497	0.00132

Phases	*P* (kbar)	*T* (°C)	Ca(Grt)	*y*(Hbl)	ca(Hbl)	*y*(Chl)	Q(Chl)	*y*(Cum)	ca(Cum)	ct(Cpx)	fs(Cpx)	Ca(Ol)
Invariant assemblages in CMASH (+Qtz + H_2O)												
Hbl, Chl, Ky, An, Zo	8.36	635.4		0.268	0.9828	0.549	0.451					
Hbl, Cum, Chl, Ky, An	7.84	662.5		0.260	0.9662	0.549	0.451	0.0209	0.055			

Phases	*P* (kbar)	*T* (°C)	Ca(Grt)	Fe(Grt)	*x*(Chl)	*y*(Chl)	Q(Chl)	*x*(Hbl)	*y*(Hbl)	ca(Hbl)	*x*(Gru)	*y*(Gru)	ca(Gru)	ca(Cpx)	ts(Cpx)	*x*(Cpx)	Fe(Ol)
Invariant assemblages in CFMASH (+Qtz + H_2O)																	
Grt, Chl, Hbl, Zo, An, Ky	8.63	647.5	0.1925	0.5489	0.2288	0.5605	0.4395	0.1954	0.3092	0.9816							
Grt, Chl, Gru, Hbl, An, Ky	8.28	663.1	0.1514	0.5335	0.2069	0.5591	0.4408	0.1766	0.2994	0.9724	0.2160	0.02420	0.04692				
Ol,Grt,Cpx,Gru,Hbl,An	4.22	725.5	0.2261	0.7165				0.6612	0.1381	0.9544	0.7427	0.01545	0.05507	0.9899	0.01787	0.7135	0.9025

contents above *c*. 0.4. Furthermore, the grid is calculated for ferrous iron phases and therefore restricted to rocks formed at low oxygen fugacities. Nevertheless for rocks containing Fe^{3+} bearing oxide minerals like hematite and magnetite, quantitative phase diagrams (*P–T* pseudosections) can be derived from the grid if the bulk rock composition is corrected for Fe^{3+}, e.g. using the procedure as outlined by Zeh (2001). The albite component in plagioclase and Na-bearing solid solutions in hornblende cannot be considered, as Na is not taken into account in our calculations. It should be noted that the addition of Na to CFMASH would extend the stability field of plagioclase-bearing assemblages to higher pressures. Furthermore, the addition of Mn can extend the garnet stability to considerably lower temperatures, because of the Mn fractionation by garnet (Mahar *et al*., 1997; Tinkham *et al*., 2001; Zeh & Holness, 2003).

In the following, quantitative phase diagrams (*P–T* pseudosections) are constructed for two grunerite–garnet-bearing rock samples (AMD & AM52), which were collected from a restricted area north of the Venetia kimberlite pipes within the Central Zone of the Limpopo Belt (Fig. 4). These rocks have intermediate to high Fe/(Fe + Mg) ratios (0.52–0.78), and low alkali- (0.3–1.6 wt.%) and Fe_2O_3-contents (0.2–1.5 wt.%) (Table 2). They are either plagioclase-free or contain anorthitic plagioclase. In addition, the two samples contain no Fe^{3+} oxide phases and Gru_{ss} has Fe/(Fe + Mg) ratios ranging between 0.51 and 0.67 (Table 2). Consequently, the mineral assemblage observed in these rocks can be well described by the CFMASH model system. It is assumed that both samples experienced similar *P–T* conditions, as they were collected from a restricted well-mapped area, which is not transected by major shear zones and/or faults (Zenglein, 2004). Consequently, the different mineral assemblages are interpreted as resulting from distinct bulk compositions (Table 2).

Petrography and mineral chemistry

Sample AMD (29°18′28.29″ N, 22°27′44.07″ E) and AM52 (29°18′27.27 N, 22°27′44.41 E) were collected from the Endora Klippe, which forms part of the Venetia Klippen Complex and occurs *c*. 3 km north of the Venetia kimberlite pipes (Fig. 4). A detailed description of the geological setting of the area surrounding the Venetia kimberlite pipes is given by Barton *et al*. (2003) and will be discussed below. Sample AMD contains the minerals garnet, grunerite, hornblende, chlorite, plagioclase, quartz, ilmenite, titanite and apatite, and sample AM52 the minerals garnet, grunerite, chlorite, ilmenite, quartz and apatite.

Garnet

Garnet porphyroblasts in sample AM52 have a maximum diameter of 2 mm and show only a slight zonation (Fig. 6b). They are commonly round, show little or no resorbtion, and contain abundant inclusions of randomly distributed chlorite, grunerite, quartz and

Fig. 2. (a) Tetrahedra showing phases and the triangular projection plane used for compatibility diagrams in the system CFMASH (with quartz + anorthite + H_2O in excess). (b) Compatibility diagrams. The numbers in the black circles are related to Fig. 1b. The numbers top right beside the respective triangular diagrams are pressures (kbar) and temperatures (°C).

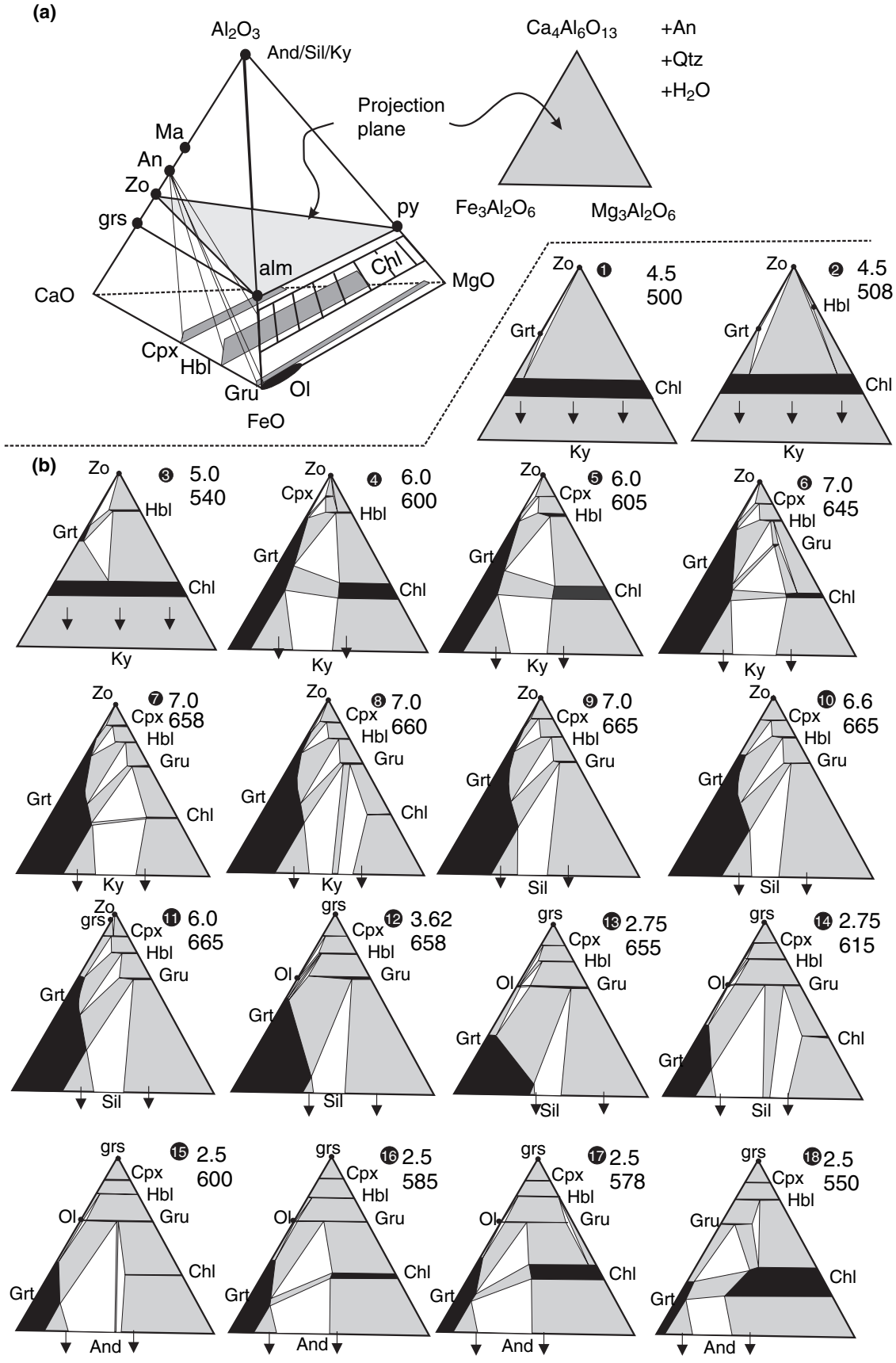

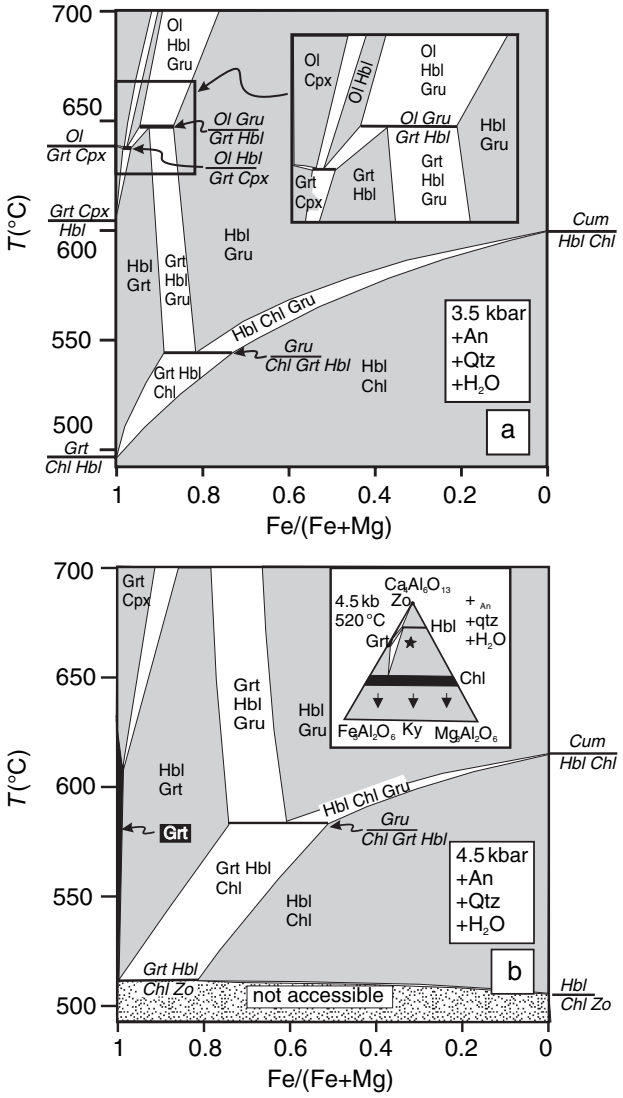

Fig. 3. T–X_{Fe} sections, showing phase relationships at (a) 3.5 kbar and (b) 4.5 kbar, for a rock with the following compositional range: CaO: 30.1, Al_2O_3: 28.9, FeO: 41.0, MgO: 0.0 ($CaO/(CaO + Al_2O_3) = 0.51$; $X_{Fe} = 1.0$) to CaO: 30.1, Al_2O_3: 28.9, FeO: 0.0, MgO: 41.0 ($X_{Fe} = 0.0$). The star in the triangular diagram in (b) represents the composition of sample AMD with $X_{Fe} = 0.52$ and $CaO/(CaO + Al_2O_3) = 0.51$.

minor ilmenite (Fig. 5a,b). In contrast, garnet grains in sample AMD are up to 4 mm in diameter and are commonly resorbed along their edges and replaced by grunerite, hornblende and plagioclase (Fig. 5e). In some places these latter three minerals form pseudomorphs after garnet. Garnet grains in sample AMD contain abundant inclusions of round quartz, lath-shaped and angular plagioclase, green hornblende and ilmenite, as well as minor chlorite and titanite (Fig. 5c,d). Furthermore the garnet shows a complex zonation pattern (Fig. 6a,c), which is characterized by a general decrease of X_{spss} [Mn/(Ca + Mg + Fe + Mn)] from core to rim (10–4 mol.%), whereas the X_{Fe}-ratio [Fe/(Fe + Mg)] is relatively constant (0.87). The X_{grs} [Ca/(Ca + Mg + Fe + Mn)] and X_{alm} [Fe/(Ca + Mg + Fe + Mn)] zonations oppose each other (Fig. 6a). In addition, there are irregularly distributed domains with high-X_{grs} and low-X_{alm} contents, disturbing the usually concentric growth zonation (Fig. 6c). There are several possible explanations for these domains. They may result from the coalescence of garnet grains, which started their growth from distinct nucleii but merged into a single porphyroblast during progressive growth. This possibility, however, is not supported by the X_{spss} zonation profile, which is unrelated to the X_{grs} peaks (Fig. 6a). Alternatively, the high-X_{grs} domains may result from domainal variations of the bulk composition, in particular of Ca, which for kinetic reasons could not be smoothed out during garnet growth and led to a local Ca disequilibrium (see Chernoff & Carlson, 1997). If correct, the irregularly distributed high-X_{grs} domains cannot be modelled by equilibrium thermodynamics, e.g. by the P–T pseudosections presented below.

The steep compositional gradients of X_{alm} and X_{grs}, as well as the decrease of $X_{spss}$from garnet core to rim of sample AMD provide evidence that the measured zonation patterns result from prograde garnet growth. The same must be concluded for garnet of sample AM52, even though it is nearly unzoned (Fig. 6b). The absence of the zonation could be explained by fast garnet growth under nearly constant P–T–X conditions, caused by a large reaction overstep (see Zeh & Holness, 2003).

Hornblende

Hornblende only occurs in sample AMD, where it is enclosed either in garnet or occurs intergrown with, or overgrown by, grunerite in the matrix (Fig. 5e,f). Hornblende inclusions in garnet are invariably round indicating hornblende consumption during garnet growth. Round and resorbed hornblende crystals are also observed in some matrix domains, where they are overgrown by euhedral grunerite (see Fig. 5f). This provides evidence that grunerite formed at the expense of hornblende, perhaps during the same hornblende-consuming reaction, which led to garnet formation. In other domains, in particular in the coronas around the resorbed garnet porphyroblasts, twinned grunerite crystals are often intergrown with hornblende and rarely with plagioclase, indicating that all three minerals were formed during garnet consumption.

Grunerite

Grunerite occurs in the matrix of both samples, either together with hornblende, plagioclase and quartz in sample AMD (Fig. 5e,f), or associated with chlorite and quartz in sample AM52 (Fig. 5a,b). In sample AM52, abundant grunerite crystals are occluded by

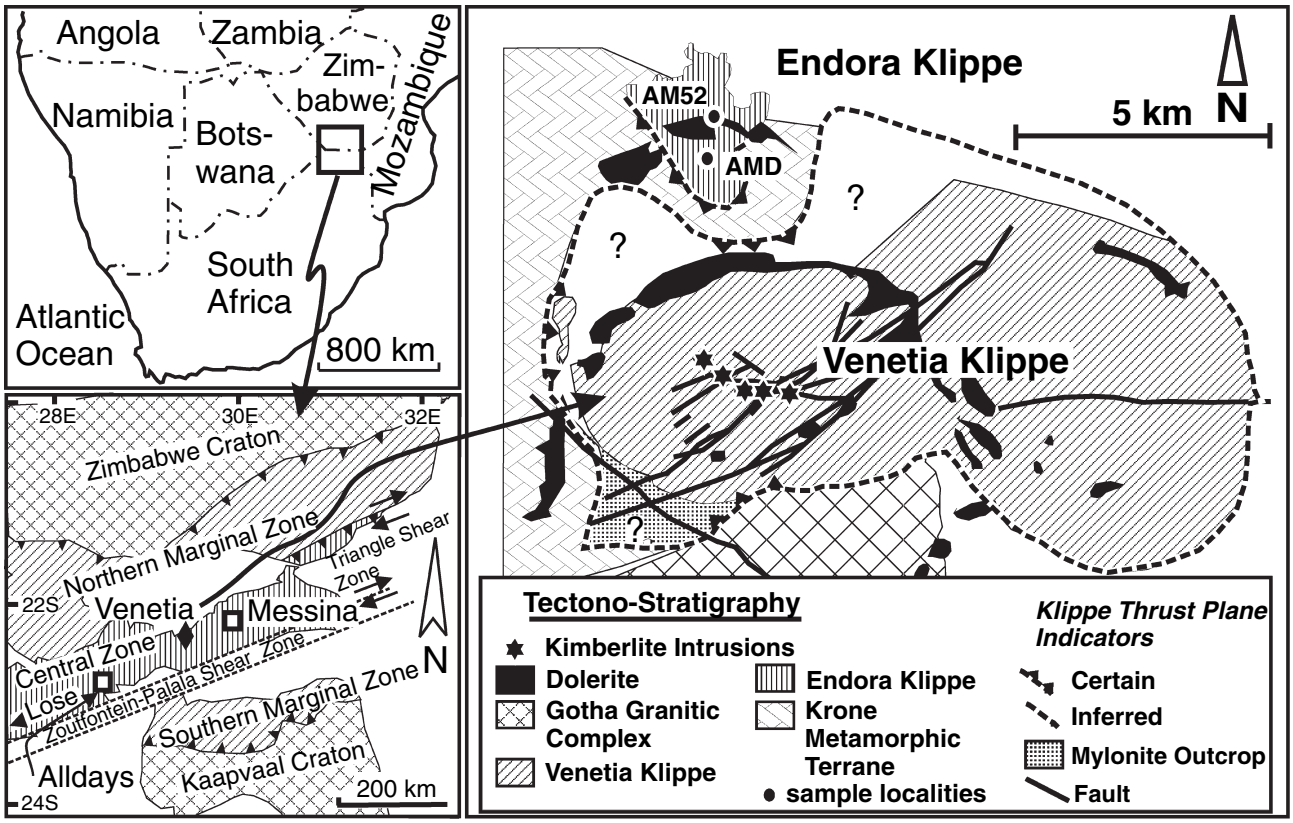

Fig. 4. Geological map showing the position and geological setting of the area surrounding the Venetia kimberlite pipes, and sample localities (modified after Barton *et al.*, 2003).

garnet, whereas no grunerite inclusions could be detected in garnet of sample AMD. This indicates that grunerite was present during growth of garnet AM52, but perhaps not during formation of the core of garnet AMD.

Hornblende and grunerite formulae were calculated water-free on the basis of 23 oxygen, using the computer program AX (T. J. B. Holland; http://www.esc.cam.ac.uk/astaff/holland/index.html). Hornblende crystals in all textural domains of sample AMD have similar X_{Mg} [Mg/(Fe + Mg)] ratios between 0.47 and 0.55 (Fig. 7a), whereas hornblende inclusions in garnet have higher silica contents (6.6–6.8 PFU) than matrix hornblende (6.3–6.7 PFU). The contents of Ti (0.068–0.113 PFU), Ca (1.784–1.830 PFU), Na (0.205–0.277 PFU) and K (0.042–0.094 PFU) scatter in the same range in all domains. In contrast to hornblende, grunerite in both rock samples shows similar silica contents between 7.8 and 7.95 PFU (Fig. 7b). However, grunerite in sample AM52 has lower X_{Mg} ratios (0.32–0.33) than in sample AMD (0.46–0.47).

Chlorite

Chlorite is widespread in sample AM52 either in the matrix in contact with garnet or as inclusions in garnet (Fig. 5a,b). However, chlorite in sample AMD occurs only as inclusions in garnet, indicating that it was present prior to and during garnet growth but reacted out just before garnet formation ceased. Chlorite in sample AM52 shows the chemical variations $Fe_{3.62-3.83}Mg_{0.68-0.90}Mn_{0-0.03}Al_{2.51-2.69}Si_{2.72-3.05}O_{10}(OH)_8$, whereas chlorite in sample AMD is more Mg-rich and has the formula $Fe_{3.22-3.14}Mg_{1.34-1.43}Mn_{0.01-0.03}Al_{2.62-2.64}Si_{2.63-2.65}O_{10}(OH)_8$.

Plagioclase

Plagioclase occurs only in sample AMD and forms either lath-shaped crystals enclosed by garnet (Fig. 5d) or round grains, which are intergrown with grunerite and hornblende in the matrix. Plagioclase in all domains is almost unzoned and anorthite-rich. Plagioclase inclusions in garnet have higher anorthite contents [$X_{an} = Ca/(Ca + Na) = 0.89$] than matrix plagioclase ($X_{an} = 0.82$).

Ilmenite

Ilmenite is rare in sample AM52, but occurs widespread in sample AMD, either enclosed in garnet or in the matrix (Fig. 5c,f). In both samples ilmenite (ilm) has only a small pyrophanite (prph) and hematite

Table 2. Representative mineral analyses and bulk compositions for sample AMD and AM52 used for geothermobarometry, and *P–T* pseudosection calculations.

	AMD-Grt				AMD-Mx					AM52-Mx				
Mineral	Grt	Chl	Hbl	Pl	Grt	Hbl	Gru	Pl	Ilm	Grt	Chl	Gru	AMD*	AM52*
SiO_2	37.26	24.19	45.68	45.80	37.10	45.88	52.72	47.30	0.07	36.75	23.11	50.27	53.91	51.26
TiO_2	0.19	0.05	0.67	0.00	0.02	0.79	0.00	0.00	52.88	0.00	0.05	0.12	0.96	0.11
Al_2O_3	21.03	20.56	10.91	34.88	21.13	10.72	0.86	33.89	0.07	20.84	20.10	1.35	16.75	8.94
Cr_2O_3	0.00	0.00	0.00	0.00	0.01	0.01	0.02	0.00	0.00	0.01	0.00	0.00		
Fe_2O_3	1.20	1.26	0.96	0.19	1.73	6.13	1.70	0.13	0.00	1.40	1.16	1.97	1.53	0.15
FeO	27.99	34.43	13.56	0.00	28.42	12.96	27.02	0.00	45.93	32.45	39.67	34.01	8.62	28.80
MnO	3.36	0.23	0.22	0.00	1.86	0.17	0.52	0.00	1.01	1.62	0.05	0.26	0.23	0.92
MgO	2.69	8.83	10.27	0.00	2.53	10.62	14.77	0.00	0.03	1.50	5.09	9.41	4.54	4.43
CaO	6.66	0.05	11.52	18.11	7.47	11.52	0.73	16.89	0.00	5.60	0.05	1.00	9.63	2.79
Na_2O	0.00	0.08	0.75	1.34	0.00	0.66	0.15	1.99	0.00	0.00	0.00	0.13	0.55	0.26
K_2O	0.00	0.03	0.32	0.03	0.00	0.34	0.04	0.03	0.00	0.00	0.00	0.03	1.11	0.04
Totals	100.39	89.71	94.86	100.35	100.27	99.80	98.53	100.23	99.99	100.18	89.28	98.55	97.82	97.70
Oxygen	12	14	23	8	12	23	23	8	3	12	14	23	CFMASH†	CFMASH†
Si	2.966	2.635	6.874	2.103	2.955	6.643	7.828	2.166	0.002	2.966	2.609	7.748		
Ti	0.011	0.004	0.076	0.000	0.001	0.086	0.000	0.000	1.002	0.000	0.004	0.014		
Al	1.973	2.640	1.935	1.888	1.984	1.830	0.151	1.829	0.002	1.983	2.675	0.245	28.9	13.5
Cr	0.000	0.000	0.000	0.000	0.001	0.001	0.002	0.000	0.000	0.001	0.000	0.000		
Fe^{3+}	0.072	0.103	0.109	0.007	0.104	0.668	0.190	0.005	0.000	0.085	0.099	0.228		
Fe^{2+}	1.864	3.136	1.706	0.000	1.893	1.569	3.355	0.000	0.967	2.190	3.746	4.384	21.1	61.8
Mn	0.227	0.021	0.028	0.000	0.125	0.021	0.065	0.000	0.022	0.111	0.005	0.034		
Mg	0.319	1.433	2.303	0.000	0.300	2.292	3.268	0.000	0.001	0.180	0.856	2.161	19.8	17.0
Ca	0.569	0.006	1.857	0.891	0.638	1.787	0.116	0.829	0.000	0.485	0.006	0.165	30.2	7.7
Na	0.000	0.017	0.219	0.119	0.000	0.185	0.043	0.177	0.000	0.000	0.000	0.039		
K	0.000	0.004	0.061	0.002	0.000	0.063	0.008	0.002	0.000	0.000	0.000	0.006		
Sum	8.000	10.000	15.169	5.010	8.000	15.146	15.026	5.007	1.996	8.000	10.000	15.024	100.00	100.00
X_{Fe}	0.85	0.69	0.43		0.86	0.41	0.51			0.92	0.81	0.67	0.52	0.78
X_{alm}	0.63				0.64					0.74				
X_{prp}	0.11				0.10					0.06				
X_{grs}	0.19				0.22					0.16				
X_{spss}	0.08				0.04					0.04				
X_{an}				0.88				0.82						

X_{Fe}, Fe/(Fe + Mg); Grt, assemblage enclosed by garnet; Mx, matrix assemblage.
*Bulk composition.
†CFMASH (mol.%) + Qtz + H_2O.

(hem) component. The ilmenite composition in sample AMD is $ilm_{0.95-0.96}prph_{0.022-0.029}hem_{0.0-0.029}$ and in sample AM52 $ilm_{0.97-0.99}prph_{0.011-0.019}hem_{0.0-0.012}$.

Titanite

Titanite was only observed as inclusions in garnet in sample AMD.

Sequence of mineral assemblages

On the basis of the observed inter- and overgrowth relationships between garnet porphyroblasts and matrix minerals, mineral inclusions in garnet, as well as garnet and hornblende resorption textures (see Fig. 5c–f), we conclude that the following mineral assemblages were successively formed in sample AMD (+quartz + ilmenite):

(AMD1) chlorite + hornblende + plagioclase;

(AMD2) garnet + chlorite + hornblende + plagioclase;

(AMD3) garnet + hornblende + grunerite + plagioclase.

In addition, textural relations reveal that garnet grew in the mineral assemblages (AMD2) and (AMD3), but was resorbed subsequently at the expense of hornblende, grunerite and plagioclase, which led to the formation of garnet pseudomorphs (Fig. 5e). As described above, the formation of garnet in sample AM52 took place in the assemblage: garnet + grunerite + chlorite + ilmenite + quartz + apatite.

THERMOBAROMETRY

Several conventional thermobarometers [computer software THERMOBAROMETRY version 2.1 of Spear & Kohn: http://ees2.geo.rpi.edu/MetaPetaRen/Frame_software.html/] and the average *P–T* feature of THERMOCALC (Holland & Powell, 1998) in combination with the computer program AX (Tim Holland; http://www.esc.cam.ac.uk/astaff/holland/index.html) were employed to obtain *P–T* information for the metamorphic evolution of these two samples (Fig. 8). The chemical composition of minerals assumed to be in equilibrium was used for the *P–T* calculation. This calculation comprised mineral assemblages enclosed by garnet AMD (AMD-Grt), the matrix of sample AMD (AMD-Mx) and the matrix of sample AM52 (AM52-

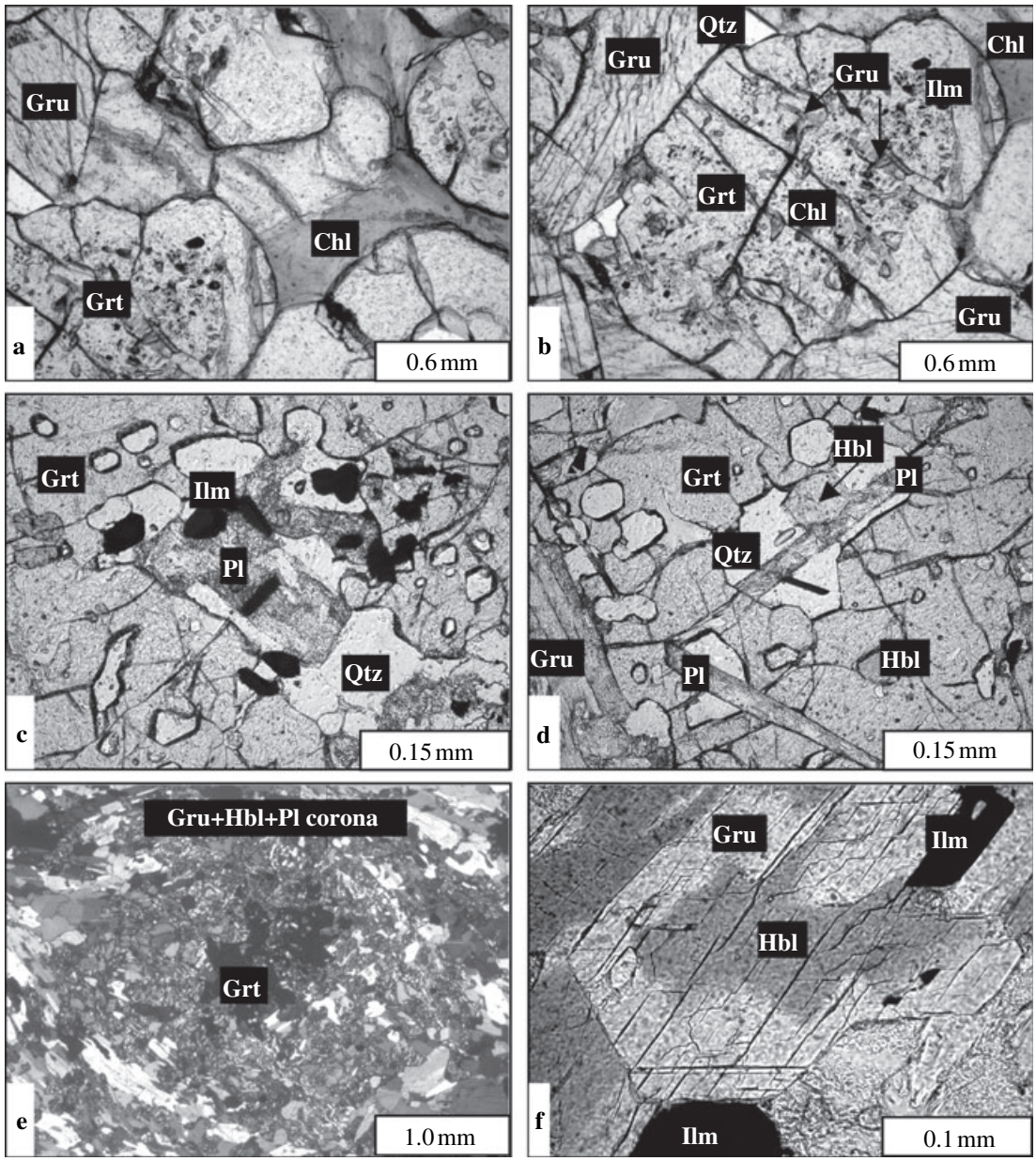

Fig. 5. Photomicrographs of sample AM52 (a, b) and sample AMD (c–f). (a) Garnet porphyroblasts (Grt) in contact with chlorite (Chl) and grunerite (Gru). (b) Garnet porphyroblast in contact with grunerite, chlorite and quartz (Qtz) showing an inclusion-rich core and inclusion-poor overgrowth. Inclusions are chlorite, grunerite and ilmenite (Ilm). (c) Garnet overgrows numerous inclusions of quartz, plagioclase (Pl) and ilmenite. (d) Lath-shaped plagioclase crystals, quartz and hornblende (Hbl) enclosed in garnet occurring in contact with grunerite. (e) Resorbed garnet porphyroblasts (black) are surrounded by a corona of grunerite, hornblende and plagioclase (crossed Nicols). (f) Resorbed hornblende crystal is overgrown by euhedral grunerite, which is in contact with ilmenite.

Mx). Analyses of these minerals are shown in Table 2, and the results of the *P–T* calculations in Table 3 and Fig. 8.

Employing the average *P–T* mode of THERMOCALC yielded *P–T* conditions of 557 ± 22 °C at 3.9 ± 1.6 kbar for assemblage AMD-Grt, and 587 ± 89 °C at 4.5 ± 1.9 kbar for assemblage AMD-Mx (Fig. 8). These conditions are higher in temperature when compared with those obtained with several thermobarometers calculated with the computer software THERMOBAROMETRY (Fig. 8). This is to be expected because the average *P–T* calculations rely more on net-transfer reactions (including dehydration reactions) and less on the cation exchange equilibria used in conventional thermometry (which are subject to resetting effects during post-metamorphic-peak cool-

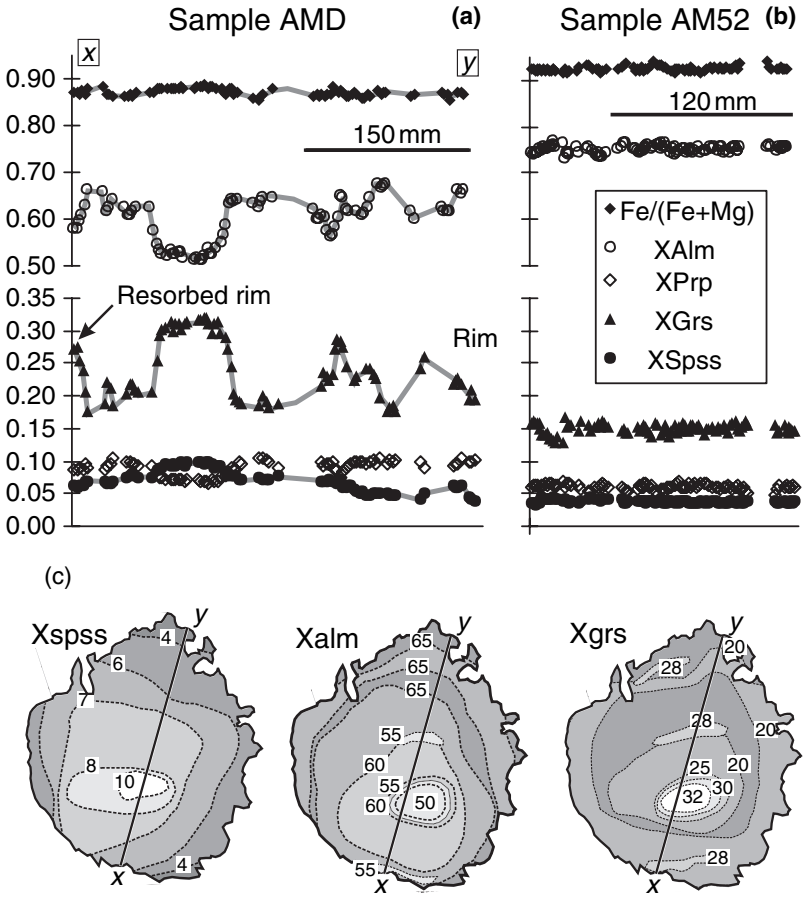

Fig. 6. Zonation profiles of garnet from sample AMD (a) and AM52 (b). (c) 2D zonation pattern of garnet AMD, reconstructed from *c*. 500 quantitative spot analyses. The profile *x*–*y* is related to (a).

ing). For the matrix assemblage AM52-Mx, temperatures of 554 ± 41 °C were calculated with the average *T* mode of THERMOCALC assuming a pressure of 4 kbar. These conditions are, within error, consistent with those obtained from sample AMD-Mx (Table 3).

P–T PSEUDOSECTIONS

In order to gain additional detailed information about the metamorphic evolution of the garnet–gruneritebearing amphibolites from the Central Zone in the Limpopo Belt, *P–T* pseudosections in the model system CFMASH were calculated (Fig. 9) and contoured for garnet composition and mode (Fig. 10a–c). The specific bulk composition used for the phase diagrams was determined by XRF-spectrometry (Philips PW 1480; Mineralogical Institute at Würzburg University) of the rock samples from which the thin sections were prepared. Fe^{2+} was analysed with a photometer (ZEISS PMD 2), using an Fe(II) −2,2′-bipyridine complex. The analyses are given in Table 2.

Sample AMD

The *P–T* pseudosection calculated for sample AMD supports the textural interpretation that the observed

Table 3. Results of *P–T* calculations.

Sample	End-members	X_{H_2O}	*T* (°C)	±2σ	*P* (kbar)	±2σ	Significant
AMD-Grt	alm, py, gr, daph, ames, tr, ts, parg, an, ab, q	1.00	547	22	3.9	1.6	1.73
		0.75	529	22	3.8	1.6	1.84
		0.50	509	23	3.7	1.7	1.96
AMD-Mx	alm, py, gr, tr, fact, parg, grun, an, ab, q	1.00	587	89	4.5	1.9	1.60
		0.75	581	81	4.3	1.8	1.50
		0.50	573	72	4.1	1.6	1.40
AM52-Mx	py, gr, alm, clin, daph, ames, cumm, grun, q	1.0	554	41	4.0	–	–

Grt, assemblage enclosed in garnet; Mx, matrix assemblage.
X_{H_2O} = mole fraction of H_2O of a mixed H_2O-CO_2 fluid.
2σ standard deviation and significant values are obtained with THERMOCALC.
End-member abbreviations are according to Holland & Powell (1998), AMD-calculated with average *P–T* feature. AM52-calculated with average *T* feature for 4 kbar.

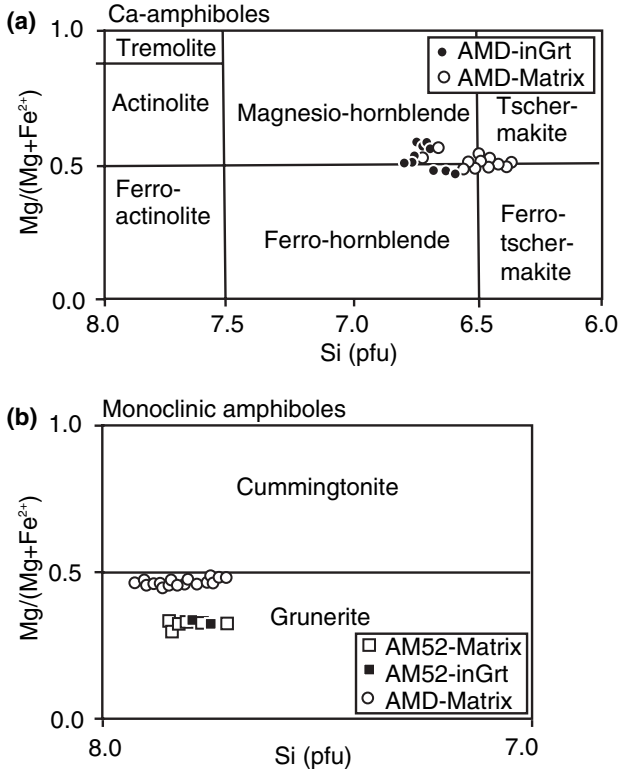

Fig. 7. Composition of hornblende (a) and grunerite (b) from samples AMD and AM52, shown in the classification diagram after Leake *et al.* (1997).

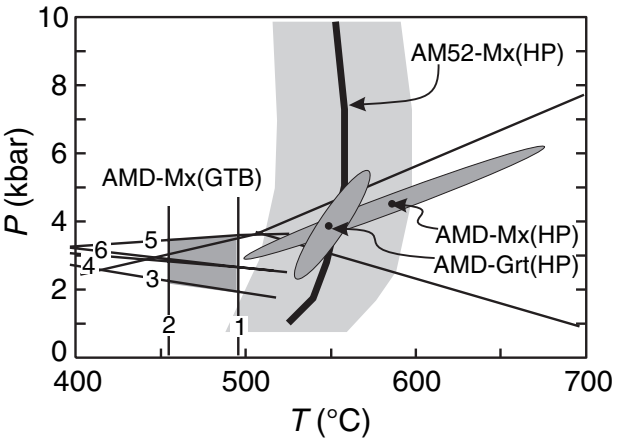

Fig. 8. Results of *P–T* calculations obtained from matrix minerals of sample AMD (AMD-Mx) and AM52 (AM52-Mx), and from minerals enclosed in garnet of sample AMD (AMD-Grt). The *P–T* calculations were carried out with the computer software THERMOCALC of Holland & Powell (1998) – (HP), and with several conventional thermobarometers using the program THERMOBAROMETRY (GTB) of Spear & Kohn (http://ees2.geo.rpi.edu/MetaPetaRen/Frame_software.html/). Mineral compositions used are shown in Table 2 and additional *P–T* results in Table 3. (1 & 2) garnet–hornblende geothermometer: (1) Graham & Powell (1984), (2) Perchuk *et al.* (1985); (3–6) Garnet–plagioclase–hornblende–quartz geobarometers: (3) Kohn & Spear (1989) – pargasite–Fe-model, (4) Kohn & Spear (1989) – pargasite–Mg-model, (5) Kohn & Spear (1990) – tschermakite–Fe-model, (6) Kohn & Spear (1990) – tschermakite–Mg-model.

assemblage sequence from (AMD1) to (AMD3) was formed during a prograde pressure and temperature increase from *c.* 570 °C at 5.5 kbar to 650 °C at 6.5 kbar (Fig. 9a). As shown in Fig. 10a, garnet will be formed along this *P–T* path (*c.* 25 mol.% Grt, normalized excluding H_2O and Qtz). X_{grs} will significantly decrease (0.28 $\rightarrow$ 0.17) during increasing pressure and temperature conditions. These features are in general agreement with the observations made in sample AMD (Figs 5 & 6). The absence of grunerite inclusions in garnet in sample AMD may be explained by garnet growth occurring predominantly in the assemblage Grt–Chl–Hbl–An, which was followed by little or no garnet formation in the assemblage Grt–Gru–Hbl–An. This interpretation is consistent with the garnet mole proportion contours shown in Fig. 10a. The contours in Fig. 10 also predict that garnet will be partially consumed when the *P–T* path progressively crosses the univariant reaction Chl + Grt + Hbl = Gru + An, until all chlorite is reacted out. Furthermore, the observed Hbl–Gru–Pl coronas around garnet may be interpreted as a result from a post-peak metamorphic pressure decrease in assemblage AMD3 (points 3–4 in Fig. 9a).

Nevertheless, the *P–T* pseudosection shown in Figs 9a and 10c cannot account for the observed X_{alm} increase from garnet core to rim from 0.50 to 0.65 (Fig. 6a,c). One reason could be that Mn, which is an important garnet component, is not considered in the CFMASH system. If Mn is taken into account and activity models for garnet and chlorite as presented in Zeh & Holness (2003) are used, the observed garnet zonation patterns may be explained more realistically. In the system MnCFMASH garnet growth will start at *c.* 30 °C lower temperatures than in CFMASH (compare Fig. 10a,d). X_{spss} and X_{grs} decrease (X_{spss} = 10–1 mol.%; X_{grs} = 28–17 mol.%) during increasing pressure and temperature conditions (Fig. 10d–g), which is in general agreement with the observed garnet growth zonation. Furthermore, X_{alm} is predicted to increase and subsequently to decrease (X_{alm} = 60 $\rightarrow$ 70 $\rightarrow$ 66 mol.%). As in the CFMASH system, garnet will be partially consumed in the assemblage Grt–Chl–Hbl–Gru–An and during a post-peak metamorphic decompression in the assemblage Grt–Gru–Hbl–An.

The *P–T* vector inferred from the *P–T* pseudosections in Figs 9 and 10 generally conforms with the results obtained by conventional thermobarometry from the domains AMD-Grt and AMD-Mx (Fig. 8), in particular with the *P–T* results calculated with the average *P–T* feature of THERMOCALC (Table 3). Within error, as propagated with THERMOCALC (see Table 3 for conventional thermobarometry and ± 30 °C and ± 1.0 kbar for *P–T* pseudosection calculations) the results are identical. Finally, it should be noted that the

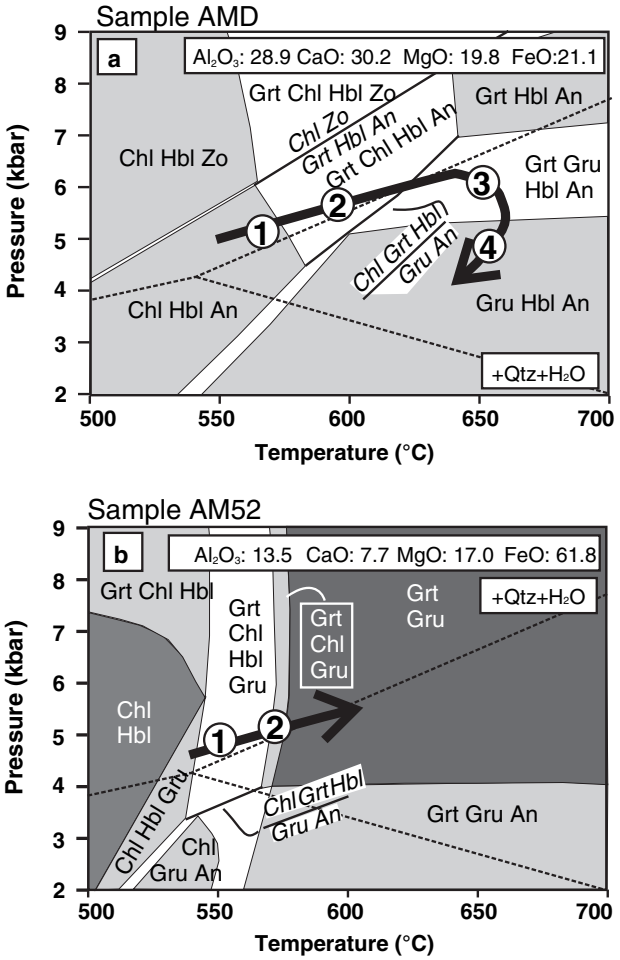

Fig. 9. *P–T* pseudosections calculated for sample AMD (a) and sample AM52 (b), using the computer software THERMOCALC version 3.1 with the dataset HP98 (Holland & Powell, 1998). The numbers represent mineral assemblages observed in thin section of the respective samples and/or described in the text. Black arrow: inferred *P–T* path.

P–T pseudosections in Fig. 10 give no explanation for the complex X_{grs} zonation patterns shown by garnet in sample AMD (Fig. 6a,c). As mentioned above, this complexity could result from kinetic effects causing local Ca-disequilibrium during garnet growth and, thus, cannot be explained by equilibrium thermodynamics.

Sample AM52

The phase diagram in Fig. 9b is consistent with the interpretation that the observed mineral assemblage Grt–Gru–Chl (AM52) was formed in a narrow temperature interval between 560 and 570 °C at pressures higher than 3.9 kbar. These *P–T* conditions are in agreement with the results obtained from the conventional geothermometry (Fig. 8), and with the *P–T* path inferred for sample AMD. According to the phase diagram in Fig. 9b it seems likely that garnet in sample AM52 crystallized initially in the assemblage Grt–Chl–Hbl–Gru, and that hornblende reacted out during the prograde evolution (points 1–2 in Fig. 9b). Consequently, hornblende is absent in the matrix.

GEOLOGICAL IMPLICATIONS

The *P–T* pseudosections and the results of conventional thermobarometry consistently support the interpretation that rocks from the Endora Klippe within the Central Zone of the Limpopo Belt underwent a contemporaneous temperature and pressure increase from *c.* 540 °C/4.5 kbar to 650 °C/6.5 kbar, followed by a post-peak metamorphic pressure decrease. Such a *P–T* path has never been inferred for rocks from the Limpopo Belt, for which the rocks are usually accepted as having all experienced granulite facies conditions (e.g. Van Reenen *et al.*, 1987; Holzer *et al.*, 1998, 1999). In fact, granulite facies rocks are widespread in the Northern and Southern Marginal Zones of the Limpopo Belt (e.g. Van Reenen, 1986; Tsunogae *et al.*, 1992; Kamber & Biino, 1995; Perchuk *et al.*, 2000), and are reported from the eastern and western parts of the Central Zone (Fig. 4); e.g. from the Messina, Alldays and Lose areas (Harris & Holland, 1984; Windley *et al.*, 1984; Droop, 1989; Hisada & Miyano, 1996; Holzer *et al.*, 1998, 1999; Van Reenen *et al.*, 2004; Zeh *et al.*, 2004). The only exception reported, so far, are rocks from the Venetia Klippe (Fig. 4), which underwent a high-grade amphibolite facies overprint with peak *P–T* conditions of 720 °C/7–8 kbar (Klemd *et al.*, 2003). Thus, the Venetia Klippen Complex, comprising the Endora Klippe seems to represent an exotic terrane within the high-grade Limpopo Belt. In order to understand its geotectonic significance, and to interpret the *P–T* path obtained from the Endora Klippe in a geological context, the following observations must be taken into consideration:

(1) The area surrounding the Venetia kimberlite pipes represents a pile of three tectono-stratigraphic units, which are separated by low-angle shear zones (Barton *et al.*, 2003). The units are named from bottom to the top: the Krone metamorphic terrane, the Venetia Klippe and the Endora Klippe (Fig. 4). U/Pb ages of detrital zircon, as well as Ar/Ar hornblende and muscovite ages provide evidence that the metasediments of the Venetia Klippe were deposited after 2.6 Ga and affected by a tectono-metamorphic overprint between 2.06 and 2.01 Ga (Barton *et al.*, 2003). Finally, these nappes were intruded by the Gotha granitic complex.

(2) The Venetia Klippen Complex is surrounded and underlain by granulite facies rocks, which are exposed in the Messina, Lose and Alldays area (e.g. Hisada & Miyano, 1996; Van Reenen *et al.*, 2004; Zeh *et al.*, 2004), and are found as xenoliths within the Venetia kimberlite pipes (Pretorius & Barton, 2003). A *P–T*

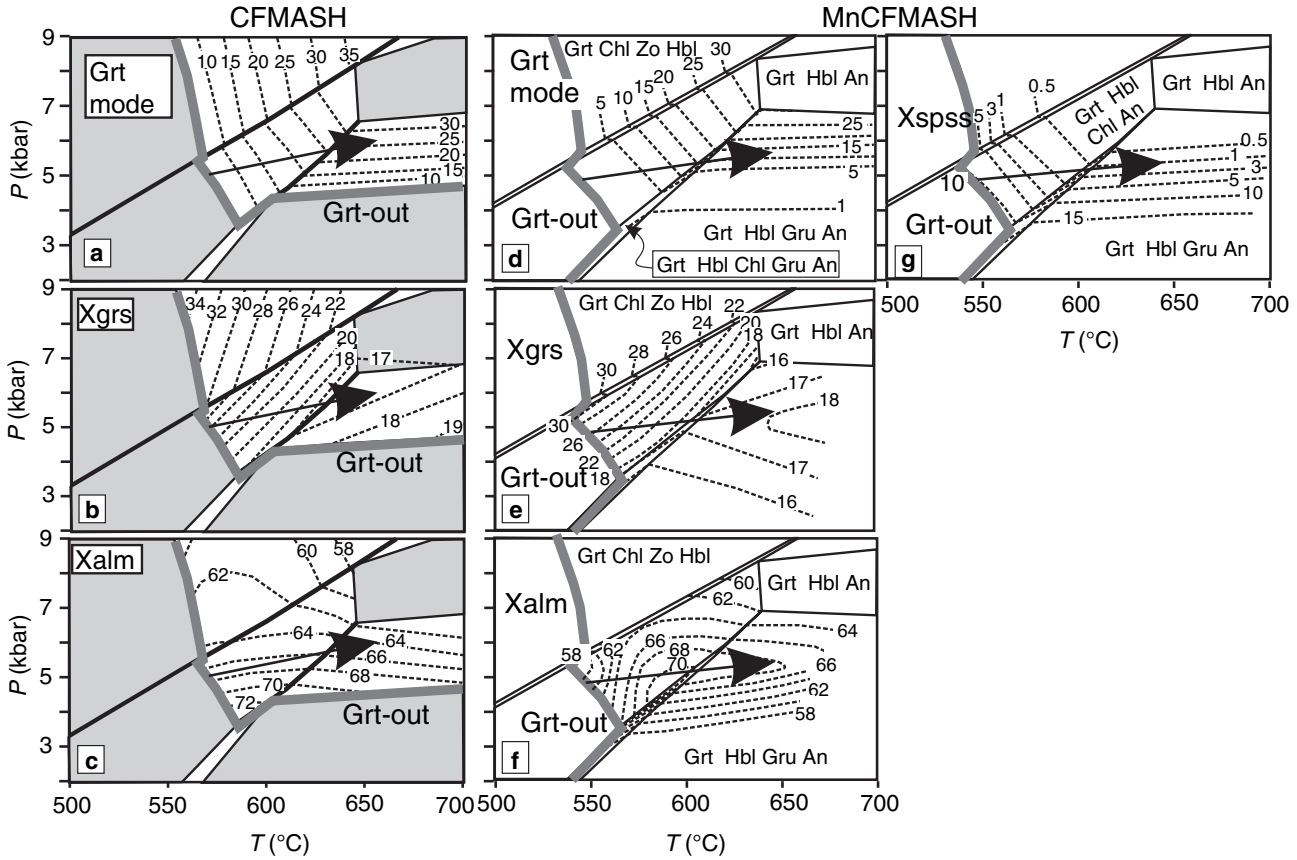

Fig. 10. *P–T* pseudosection for sample AMD calculated in the system CFMASH (a–c), and MnCFMASH (d–g), contoured for the garnet mode (a, d), X_{grs} (b, e), X_{alm} (c, f), and X_{spss} (g). The grey lines and phase fields in (a–c) are related to Fig. 9a. The black arrows represent a *P–T* path that best explains the observed garnet growth zonation. Composition used for the *P–T* pseudosection in Fig. 10d–g is: Al_2O_3: 28.86, CaO: 30.16, MgO: 19.81, FeO: 21.11, MnO: 0.06 (for further explanations see text).

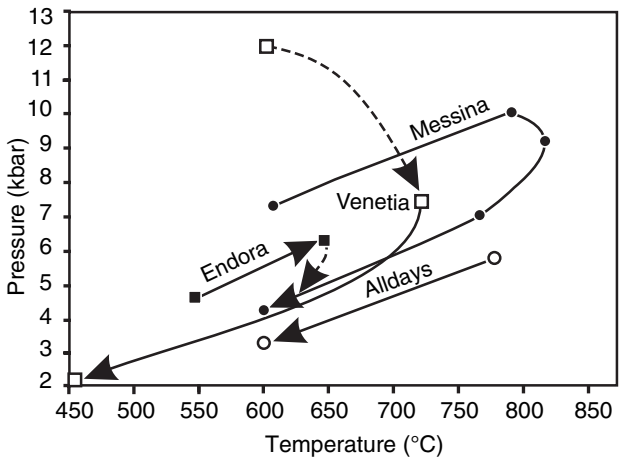

Fig. 11. Synopsis of *P–T* paths inferred from different areas within the Central Zone of the Limpopo Belt; Venetia Klippe: Klemd *et al.* (2003); Endora Klippe: this study; Messina area: Zeh *et al.* (2004); Alldays area: Van Reenen *et al.* (2004).

path inferred from granulite facies rocks of the Messina area (*c.* 60 km east of Venetia) indicates that the granulites underwent a prograde temperature and pressure increase from 600 °C/7 kbar to 780 °C/9–10 kbar (pressure peak) to 820 °C/8 kbar (thermal peak), followed by a decompression-cooling path to 600 °C/4 kbar (Zeh *et al.*, 2004; Fig. 11). A similar retrograde *P–T* path is reported from the Alldays area, *c.* 100 km west-southwest of Venetia (Van Reenen *et al.*, 2004; Fig. 11). The prograde *P–T* path suggests that the granulites of the Messina area were formed during contemporaneous burial and heating, maintained by a combination of crustal stacking on top and thermal relaxation at depth (Zeh *et al.*, 2004). Geochronological results of Barton *et al.* (1983); Jaeckel *et al.* (1997) and Holzer *et al.* (1998) support the timing of the thermal peak during granulite facies metamorphism at *c.* 2.03 Ga and that subsequent cooling occurred until 1.98 Ga. Garnet with relic growth zonation additionally indicates that the granulites in the Messina area underwent a fast prograde heating and cooling during a single orogenic event (Zeh *et al.*, 2004).

The geochronological and petrological evidence from the Messina area and the Venetia Klippen Complex indicates that granulite and amphibolite facies metamorphism in the Central Zone were coeval

at *c*. 2.03 Ga, i.e. much later than the granulite facies metamorphism which affected the Northern and Southern Marginal Zones at *c*. 2.7 Ga (e.g. Van Reenen, 1986; Tsunogae *et al*., 1992; Berger *et al*., 1995; Mkweli *et al*., 1995; Kreissig *et al*., 2001). At present, there is no unambiguous evidence for a regional metamorphic event in the Central Zone prior to 2.06 Ga, even though several ages of *c*. 2.6 Ga and 3.1 Ga are reported (e.g. Jaeckel *et al*., 1997; Kröner *et al*., 1999; Boshoff, 2004). However, most of these ages were obtained from magmatic zircon and could reflect the time of granite emplacement. Hard evidence for a metamorphic event at *c*. 2.52 Ga is presented only by the dating of metamorphic garnet and sillimanite, obtained from metapelitic xenoliths within the Bulai batholith. However, these mineral ages do not necessarily reflect the time of an important regional metamorphic event, as suggested by Holzer *et al*. (1998), but may rather be interpreted as representing the age of the contact metamorphic overprint.

The prograde *P–T* path inferred for the rocks from the Endora Klippe (Fig. 11) is consistent with crustal stacking and heating. In fact, the *P–T* vector is similar to that obtained from the granulites of the Messina area (Fig. 11), but is shifted to lower pressure and temperature conditions. Thus, we conclude that the inferred *P–T* path of the Endora Klippe reflects the metamorphic evolution in the roof zone of the granulites now exposed in the surrounding areas. The low angle shear zones that separate the different nappes of the Venetia Klippen Complex also support a conclusion that burial of the granulite facies rocks was achieved by horizontal nappe tectonics, which caused successive stacking of rock units on the top of the Central Zone. The only argument against such a simple model is a prograde *P–T* path inferred from rocks of the Venetia Klippe (Fig. 11), which indicates a prograde *P–T* decrease from 630 °C/13 kbar to 720 °C/7–8 kbar (Klemd *et al*., 2003), and not a prograde pressure increase as inferred for the Endora Klippe rocks. Thus, either the prograde *P–T* path inferred by Klemd *et al*. (2003) for the Venetia Klippe is erroneous because of disequilibrium thermobarometry or rocks of the Venetia and Endora Klippe underwent different *P–T* evolutions and came into juxtaposition late during the tectono-metamorphic history. In order to obtain more information on this important problem, additional petrological and geochronological work in the Limpopo Central Zone is required.

CONCLUSIONS

(1) The results of this study indicate that quantitative phase diagrams derived from a calculated petrogenetic grid in the system CFMASH adequately explain mineral assemblages, textures and compositional trends observed in garnet–grunerite-bearing amphibolites.

(2) The petrological results indicate that rocks from the Endora Klippe within the Central Zone of the Limpopo Belt experienced only amphibolite facies metamorphism during a contemporaneous temperature and pressure increase from *c*. 540 °C/4.5 kbar to 650 °C/6.5 kbar, followed by a post-peak metamorphic pressure decrease.

(3) The inferred *P–T* path, in combination with geochronological and petrological data from surrounding areas, supports a tectonic model which suggests that the rocks from the Endora Klippe reflect the metamorphic evolution in the roof zone of the migmatitic gneisses and granulites exposed widely in the Central Zone. They also suggest that granulite and amphibolite facies metamorphism occurred during the Palaeoproterozoic at *c*. 2.03 Ga.

ACKNOWLEDGEMENTS

This paper benefited from discussions with J. Barton (Rand Afrikaans University, Johannesburg) and R. Zenglein (University Würzburg). Their help in the field is highly appreciated. We are furthermore indebted to the Venetia mine and DeBeers Consolidated Mines, who financially and logistically supported our fieldwork. We also thank R. White (University Melbourne) and D. Tinkham (University Calgary) for helpful reviews and M. Brown for editorial handling.

REFERENCES

Barton, J.M., Ryan, B. & Fripp, R.E.P., 1983. Rb–Sr and U–Th–Pb studies of the Sand River Gneisses, Central Zone, Limpopo Mobile Belt. *Geological Society of South Africa, Special Publication*, **8,** 9–18.

Barton, J.M., Barnett, W., Barton, E.S. *et al*. 2003. The geology of the area surrounding the Venetia kimberlite pipes, Limpopo Belt, South Africa: a complex assembly of terranes and granitoid magmatism. *South African Journal of Geology*, **106,** 109–128.

Berger, M., Kramers, J.D. & Nägler, T., 1995. Geochemistry and geochronology of charnoenderbitic rocks in the Northern Marginal Zone of the Limpopo Belt, southern Africa, and genetic models. *Schweizerische Mineralogische und Petrographische Mitteilungen*, **75,** 17–42.

Boshoff, R., 2004. Formation of major fold types during distinct geological events in the Central Zone of the Limpopo Belt, South Africa: new structural, metamorphic and geochronological data. MSc Thesis, Rand Afrikaans University, Johannesburg, South Africa. pp. 121.

Chernoff, C.B. & Carlson, W.D., 1997. Disequilibrium for Ca during growth of pelitic garnet. *Journal of Metamorphic Geology*, **15,** 421–438.

Droop, G.T.R., 1989. Reaction history of garnet-sapphirine granulites and conditions of Archaean high-pressure granulite-facies metamorphism in the Central Limpopo Mobile Belt, Zimbabwe. *Journal of Metamorphic Geology*, **7,** 383–403.

Ernst, W.G., 1966. Synthesis and stability relations of ferrotremolite. *American Journal of Science*, **264,** 37–65.

Evans, B.W. & Ghiorso, M.S., 1995. Thermodynamics and petrology of cummingtonite. *American Mineralogist*, **80,** 649–663.

Fonarev, V.I. & Korolkov, G.Y., 1980. The assemblage orthopyroxene + cummingtonite + quartz. The low temperature stability limit. *Contributions to Mineralogy and Petrology*, **73,** 413–420.

Fonarev, V.I., Korolkov, G.Y. & Dokina, T.N., 1977. Experimental study in the assemblage orthopyroxene + olivine + quartz. In: *Problems of Physico-chemical Petrology*, 1. pp. 159–171. Nauka, Moscow, Russia.

Fonarev, V.I., Korolkov, G.Y. & Dokina, T.N., 1979. Laboratory data on the stability field of the cummingtonite + olivine + quartz association. *Geochemistry International*, **16,** 21–32.

Gole, M.J. & Klein, C., 1981. High-grade metamorphic Archaean banded iron-formations, Western Australia: assemblages with coexisting pyroxenes ± fayalite. *American Mineralogist*, **66,** 87–99.

Graham, C.M. & Powell, R., 1984. A garnet–hornblende geothermometer: calibration, testing, and applications to the Pelona Schist, South California. *Journal of Metamorphic Geology*, **2,** 13–21.

Harris, N.B.W. & Holland, T.J.B., 1984. The significance of cordierite–hypersthene assemblages from the Beitbridge region of the Central Limpopo Belt: evidence for rapid decompression in the Archaean? *American Mineralogist*, **69,** 1036–1049.

Hisada, K. & Miyano, T., 1996. Petrology and microthermometry of aluminous rocks in the Botswanan Limpopo Central Zone: evidence for isothermal decompression and isobaric cooling. *Journal of Metamorphic Geology*, **14,** 183–197.

Hoinkes, G. & Mogessi, A., 1986. Coexisting cummingtonite and calcic amphibole in amphibolites from the Schneeberg Complex, Tyrol, Austria. *Tschermaks Mineralogische und Petrologische Mitteilungen*, **35,** 33–45.

Holland, T.J.B. and Powell, R., 1996a. Thermodynamics of order-disorder in Minerals 1: symmetric formalism applied to minerals of fixed composition. *American Mineralogist*, **81,** 1413–1424.

Holland, T.J.B. & Powell, R., 1996b. Thermodynamics of order-disorder in Minerals 2: symmetric formalism applied to solid solutions. *American Mineralogist*, **81,** 1425–1437.

Holland, T.J.B. & Powell, R., 1998. An internally consistent thermodynamic data set of phases of petrological interest. *Journal of Metamorphic Geology*, **16,** 309–343.

Holland, T.J.B., Baker, J.M. & Powell, R. 1998. Mixing properties and activity–composition relationships of chlorites in the system MgO–FeO–Al_2O_3–SiO_2–H_2O. *European Journal of Mineralogy*, **10,** 395–406.

Hollocher, K., 1991. Prograde amphibole dehydration reactions during high-grade regional metamorphism, central Massachusetts, U.S.A. *American Mineralogist*, **76,** 956–970.

Holzer, L., Frei, R., Barton, J.M. & Kramers, J.D., 1998. Unraveling the record of successive high grade events in the Central Zone of the Limpopo Belt using Pb single phase dating of metamorphic minerals. *Precambrian Research*, **87,** 87–115.

Holzer, L., Barton, J.M., Paya, B.K. & Kramers, J.D., 1999. Tectonothermal history in the western part of the Limpopo Belt: test of tectonic models and new perspectives. *Journal of African Earth Sciences*, **28,** 383–402.

Immega, I.P. & Klein, C., 1976. Mineralogy and petrology of some metamorphic Precambrian iron-formations in southwestern Montana. *American Mineralogist*, **61,** 1117–1144.

Jaeckel, P., Kröner, A., Kamo, S.L., Brandl, G. & Wendt, J.I., 1997. Late Archaean to early Proterozoic granitoid magmatism and high-grade metamorphism in the central Limpopo belt, South Africa. *Journal of the Geological Society of London*, **154,** 25–44.

Kamber, B.S. & Biino, G.G., 1995. The evolution of high-*T* low-*P* granulites in the Northern Marginal Zone sensu stricto, Limpopo belt, Zimbabwe – the case for petrography. *Schweizerische Mineralogische und Petrographische Mitteilungen*, **75,** 427–454.

Kenah, C. & Hollister, L., 1983. Anatexis in the Central Gneiss Complex, British Columbia. In: *Migmatites, Melts and Metamorphism*. (eds. Atherton, M. & Gribble, C.), pp. 142–161. Nantwich, Cheshire, UK.

Klein, C., 1966. Mineralogy and petrology of the metamorphosed Wabush Iron Formation, southwestern Labrador. *Journal of Petrology*, **7,** 246–305.

Klemd, R., Schmidt, A., Martin, J. & Barton, J.M., 2003. *P–T* path constraints from metapelitic rocks east of the Venetia kimberlite pipes, Central Zone, Limpopo Belt, South Africa: Have these rocks seen granulite-facies conditions? *South African Journal of Geology*, **106,** 129–148.

Kohn, M.J. & Spear, F.S., 1989. Empirical calibration of geobarometers for the assemblage garnet + hornblende + plagioclase + quartz. *American Mineralogist*, **74,** 77–84.

Kohn, M.J. & Spear, F.S., 1990. Two new barometers for garnet amphibolites with application to southeastern Vermont. *American Mineralogist*, **75,** 89–96.

Kreissig, K., Holzer, L., Frei, R. *et al*. 2001. Geochronology of the Hout River Shear Zone and the metamorphism in the Southern Marginal Zone of the Limpopo Belt, Southern Africa. *Precambrian Research*, **109,** 145–173.

Kretz, R., 1983. Symbols for rock forming minerals. *American Mineralogist*, **68,** 277–279.

Kröner, A., Jaeckel, P., Brandl, G., Nemchin, A.A. & Pidgeon, R.T., 1999. Single zircon ages for granitoid gneisses in the Central Zone of the Limpopo Belt, Southern Africa and geodynamic significance. *Precambrian Research*, **93,** 299–337.

Lattard, D. & Evans, B.W., 1992. New experiments on the stability of grunerite. *European Journal of Mineralogy*, **4,** 219–238.

Leake, B.E., Wooley, A.R., Arps, C.E.S. *et al*. 1997. Nomenclature of amphiboles. *European Journal of Mineralogy*, **9,** 623–651.

Mahar, E.M., Baker, J.M., Powell, R., Holland, T.J.B. & Howell, N., 1997. The effect of Mn on mineral stability in metapelites. *Journal of Metamorphic Geology*, **15,** 223–238.

Miyano, T. & Klein, C., 1983. Phase relations of orthopyroxene, olivine, and grunerite in high-grade metamorphic iron-formations. *American Mineralogist*, **68,** 699–716.

Miyano, T. & Klein, C., 1986. Fluid behaviour and phase relations in the system Fe–Mg–Si–C–O–H: application to high grade metamorphism of iron-formations. *American Journal of Science*, **286,** 540–575.

Mkweli, S., Kamber, B. & Berger, M., 1995. Westward continuation of the craton – Limpopo Belt tectonic break in Zimbabwe and new age constraints on the timing of the thrusting. *Journal of the Geological Society of London*, **152,** 77–83.

Mottana, A., Bocchio, R., Crespi, R., DeCapitani, L., Liborio, G. & Ventura, G.D., 1994. Cummingtonite in the amphibolites of the South-Alpine Basement Complex (Upper Lake Como region, Italy): its relationships with hornblende. *Mineralogy and Petrology*, **51,** 67–84.

Perchuk, L.L., Aranovich, L.Y. & Podlesskii, K.K. *et al*. 1985. Precambrian granulites of the Aldan shield, eastern Siberia, USSR. *Journal of Metamorphic Geology*, **3,** 265–310.

Perchuk, L.L., Gerya, T.V., van Reenen, D.D. *et al*. 2000. Comparative petrology and metamorphic evolution of the Limpopo (South Africa) and Lapland (Fennoscandia) high-grade terrains. *Mineralogy and Petrology*, **69,** 69–107.

Powell, R. & Holland, T.J.B., 1999. Relating formulations of the thermodynamics of mineral solid solutions: activity modelling of pyroxenes, amphiboles and micas. *American Mineralogist*, **84,** 1–14.

Pretorius, W. & Barton, J.M., 2003. Petrology and geochemistry of crustal and upper mantle xenoliths from the Venetia Diamond Mine – evidence for Archean crustal growth

and subduction. *South African Journal of Geology*, **106,** 213–230.
Tinkham, D.K., Zulaga, C.A. & Stowell, H.H., 2001. Metapelite phase equilibria modeling in MnNCKFMASH: The effect of variable Al_2O_3 and MgO/(MgO + FeO) on mineral stability. *Geological Material Research*, **3,** 2–42.
Tsunogae, T., Miyano, T. & Ridley, J., 1992. Metamorphic *P–T* profiles from Zimbabwe Craton to the Limpopo belt. *Precambrian Research*, **55,** 259–278.
Van Reenen, D.D., 1986. Hydration of cordierite and hypersthene and description of the retrograde orthoamphibole isograde in the Limpopo Belt, South Africa. *American Mineralogist*, **71,** 900–915.
Van Reenen, D.D., Barton, J.M., Roering, C., Smit, C.A. & Van Schalkwyk, J.F., 1987. Deep crustal response to continental collision: the Limpopo Belt of Southern Africa. *Geology*, **15,** 11–14.
Van Reenen, D.D., Perchuk, L.L., Smit, C.A. *et al.* 2004. Structural and *P–T* evolution of a major cross fold in the Central Zone of the Limpopo high-grade terrain, South Africa. *Journal of Petrology*, **45,** 1413–1439.
White, R.W., Powell, R., Holland, T.J.B. & Worley, B.A., 2000. The effect of TiO_2 and Fe_2O_3 on metapelitic assemblages at greenschist and amphibolite facies conditions: mineral equilibria calculations in the system K_2O–FeO–MgO–Al_2O_3–SiO_2–H_2O–TiO_2–Fe_2O_3. *Journal of Metamorphic Geology*, **18,** 497–511.
Windley, B.F., Ackermand, D. & Herd, R.K., 1984. Sapphirine/kornerupine-bearing rocks and crustal uplift history of the Limpopo belt, Southern Africa. *Contributions to Mineralogy and Petrology*, **86,** 342–358.
Zeh, A., 2001. Inference of a detailed *P–T* path from *P–T* pseudosections using metapelitic rocks of variable composition from a single outcrop, Shackleton Range, Antarctica. *Journal of Metamorphic Geology*, **19,** 329–350.
Zeh, A. & Holness, M., 2003. The effect of reaction overstep on garnet microtextures in metapelitic rocks of the Ilesha Schist Belt, SW Nigeria. *Journal of Petrology*, **44,** 967–994.
Zeh, A., Klemd, R., Buhlmann, S. & Barton J.M., 2004. Pro- and retrograde *P–T* evolution of granulites of the Beit Bridge Complex (Limpopo Belt, South Africa): constraints from quantitative phase diagrams and geotectonic implications. *Journal of Metamorphic Geology*, **22,** 79–95.
Zenglein R., 2004. Geological and mineralogical investigations on an area north of the Venetia Diamond Mine (South Africa). Diploma Thesis, pp. 157. Würzburg University, Germany.

Received 30 June 2004; revision accepted 11 November 2004.

APPENDIX

Thermodynamic data, solid solutions, site fractions and activity expressions

The data for ferroactinolite and cummingtonite end-members in the dataset of Holland & Powell (1998) require modification. The cummingtonite data were based on an assumption of ideal mixing in olivine, orthopyroxene and grunerite equilibrated in the experiments of Fonarev *et al.* (1979); because the phases are quite Fe-rich and somewhat non-ideal, extrapolation to cummingtonite is unsatisfactory. For simplicity, in this study the mixing properties of olivine, orthopyroxene and grunerite are treated as simple regular solutions such that they simulate the activity–composition relations in the more extensive order–disorder treatments (see Holland & Powell, 1996a,b). The mixing relations are detailed below, including an enthalpy adjustment of −22.2 kJ relative to the data in Holland & Powell (1998) for cummingtonite.

Also, as argued in Evans & Ghiorso (1995), ferroactinolite appears to be more stable than implied by the experiments of Ernst (1966) and therefore its thermodynamic data require adjustment. Because non-ideal solution models are used here, there are relationships between the end-member Gibbs energies and the regular solution model interaction energies, particularly through the internal equilibria such as 7 tr + 5 grn = 7 fact + 5 cum as discussed in Powell & Holland (1999). We have derived an internally consistent set of interaction energy parameters for the amphibole end-members:

W_{ij} (kJ)	tr	ts	fac	cum	fts	grn
tr	*	20	9	45	32.9	80.4
ts		*	12.9	n	3.2	n − 12.8
fac			*	41.4	15	51.5
cum				*	n + 5.3	17.6
fts					*	n + 3.0
grn						*

These are based on assumed values for W(tr,fac) and W(tr,cum), derived by analogy with other Fe–Mg mixing systematics (Holland & Powell, 1998, p. 318; Powell & Holland, 1999, p. 8–10) and on the width of the actinolite–grunerite solvus. W(tr,ts) was taken from Holland & Powell (1998). The internal equilibrium yields the constraints:

$$H(\text{fac}) = H(\text{tr}) + \frac{5}{7}H(\text{grn}) - \frac{5}{7}H(\text{cum}) + \text{delta}$$

where

$$\text{delta} = -\frac{7}{5}W(\text{tr,fac}) + W(\text{fac,cum}) - W(\text{tr,cum})$$

and

$$W(\text{tr,grn}) = \frac{84}{25}W(\text{tr,fac}) + \frac{60}{25}W(\text{tr,cum}) - \frac{35}{25}W(\text{fac,cum})$$

$$W(\text{cum,grn}) = \frac{49}{25}W(\text{tr,fac})$$

$$W(\text{grn,fac}) = \frac{14}{25}W(\text{tr,fac}) + \frac{35}{25}W(\text{tr,cum}) - \frac{10}{25}W(\text{fac,cum})$$

Taken together these provide values for W(fac,cum) and W(grn,fac). Similar reasoning leads to the other values in the table above, with an unknown value (=n above) for W(cum,ts). The value for n was estimated to be around 125 kJ by adjustment until agreement with the alumina content of natural grunerites was obtained. The properties of fact are derived from those of tremolite, grunerite and cummingtonite using the relationships above and require a value for delta of 15.9 kJ [i.e. −5/7 (22.2) kJ] and hence a Gibbs energy increment of 38.1 kJ relative to the data in Holland & Powell (1998).

For clinopyroxene, similar arguments allow a simple model among the end-members diopside, hedenbergite, Ca-Tschermaks pyroxene and clinoenstatite. The interaction energies are listed below and are based on the Cpx–Opx miscibility gap, Fe–Mg–Al exchange between pyroxenes and garnet. The Gibbs energy increment, given below (8.1–0.0045T kJ) allows for the ortho = clino transition in enstatite.

To reproduce the results of this study accurately requires the data files used here, which may be obtained from the first author on request.

Olivine (Ol): $(Fe,Mg)_2SiO_4$

Mineral end-members:

$$\text{Fayalite (fa)} : Fe_2SiO_4$$

$$\text{Fosterite (fo)} : Mg_2SiO_4$$

Compositional variable:

$$x = \text{Fe(Ol)} = \text{Fe}/(\text{Fe} + \text{Mg})$$

Ideal mixing on site activity expressions:

$$x = \mathrm{Fe(Ol)} = \mathrm{Fe}/(\mathrm{Fe} + \mathrm{Mg})$$

$$a(\mathrm{fa}) = x(\mathrm{Fe})^2$$

$$a(\mathrm{fo}) = x(\mathrm{Mg})^2$$

Regular solution parameters: $W(\mathrm{fa,fo}) = 9$ kJ

Clinopyroxene (Cpx): $(Ca,Mg)^{M2}$ $(Fe,Mg,Al)^{M1}$ $(Al,Si)^{T2}$ Si^{T1} O_6

Mineral end-members:

$$\text{Diopside (di)} : CaMgSi_2O_6$$

$$\text{Hedenbergite (hed)} : CaFeSi_2O_6$$

$$\text{Ca-Tschermaks Px (cats)} : CaAlAlSiO_6$$

$$\text{Enstatite (en)} : Mg_2Si_2O_6$$

Compositional variables:

$\mathrm{Ca(Cpx)} = X\mathrm{Ca,M2}$ $\mathrm{ts(Cpx)} = X\mathrm{Al,M1}$ $x(\mathrm{Cpx}) = \mathrm{Fe}/(\mathrm{Fe} + \mathrm{Mg})$

Ideal mixing on site activity expressions:

$$x(\mathrm{Ca,M2}) = \mathrm{Ca} \quad x(\mathrm{Mg,M2}) = (1-x)(1-\mathrm{Ca})$$

$$x(\mathrm{Al,M1}) = \mathrm{ts} \quad x(\mathrm{Fe,M1}) = x(1-\mathrm{ts}) \quad x(\mathrm{Mg,M1}) = (1-x)(1-\mathrm{ts})$$

$$a(\mathrm{di}) = x(\mathrm{Ca,M2})x(\mathrm{Mg,M1})$$

$$a(\mathrm{hed}) = x(\mathrm{Ca,M2})x(\mathrm{Fe,M1})$$

$$a(\mathrm{cats}) = x(\mathrm{Ca,M2})x(\mathrm{Al,M1})$$

$$a(\mathrm{en}) = x(\mathrm{Mg,M2})x(\mathrm{Mg,M1})$$

Regular solution parameters:

$W(\mathrm{di,hed}) = 2.5$, $W(\mathrm{di,cats}) = 7$, $W(\mathrm{di,en}) = 24$,
$W(\mathrm{hed,cats}) = 4$, $W(\mathrm{hed,en}) = 34$, $W(\mathrm{cats,en}) = 24$ kJ

Gibbs energy increment: $\mathrm{DQF(en)} = 8.1\text{–}0.0045T$ kJ

Grunerite (Gru): $(Ca,Fe,Mg)_2^{M4}(Fe,Mg)_3^{M13}(Fe,Mg,Al)_2^{M2}$ $(Al,Si)_2^{T1}Si_6O_{22}(OH)_2$

Mineral end-members:

$$\text{Tremolite (tr)} : Ca_2Mg_5Si_8O_{22}(OH)_2$$

$$\text{Ferroactinolite (fact)} : Ca_2Fe_5Si_8O_{22}(OH)_2$$

$$\text{Tschermakite (ts)} : Ca_2Mg_3Al_2Al_2Si_6O_{22}(OH)_2$$

$$\text{Cummingtonite (cum)} : Mg_7Si_8O_{22}(OH)_2$$

Compositional variables:

$x(\mathrm{Gru}) = \mathrm{Fe}/(\mathrm{Fe} + \mathrm{Mg})$ $y(\mathrm{Gru}) = X\mathrm{Al,M2}$ $\mathrm{ca(Gru)} = X\mathrm{Ca,M4}$

Ideal mixing on site activity expressions:

$$x(\mathrm{Ca,M4}) = \mathrm{Ca} \quad x(\mathrm{Fe,M4}) = x(1-\mathrm{ca})$$
$$x(\mathrm{Mg,M4}) = (1-x)(1-\mathrm{ca})$$

$$x(\mathrm{Fe,M13}) = x \quad x(\mathrm{Mg,M13}) = (1-x)$$

$$x(\mathrm{Fe,M2}) = x(1-y) \quad x(\mathrm{Mg,M2}) = (1-x)(1-y) \quad x(\mathrm{Al,M2}) = y$$

$$x(\mathrm{Al,T1}) = \frac{1}{2}y \quad x(\mathrm{Si,T1}) = 1 - \frac{1}{2}y$$

$$a(\mathrm{tr}) = x(\mathrm{Ca,M4})^2 x(\mathrm{Mg,M13})^3 x(\mathrm{Mg,M2})^2 x(\mathrm{Si,T1})^2$$

$$a(\mathrm{fact}) = x(\mathrm{Ca,M4})^2 x(\mathrm{Fe,M13})^3 x(\mathrm{Fe,M2})^2 x(\mathrm{Si,T1})^2$$

$$a(\mathrm{ts}) = 4x(\mathrm{Ca,M4})^2 x(\mathrm{Mg,M13})^3 x(\mathrm{Al,M2})^2 x(\mathrm{Al,T1}) x(\mathrm{Si,T1})$$

$$a(\mathrm{cum}) = x(\mathrm{Mg,M4})^2 x(\mathrm{Mg,M13})^3 x(\mathrm{Mg,M2})^2 x(\mathrm{Si,T1})^2$$

Regular solution parameters:

$W(\mathrm{tr,fact}) = 9$, $W(\mathrm{tr,ts}) = 20$, $W(\mathrm{tr,cum}) = 45$,
$W(\mathrm{fact,ts}) = 12.9$, $W(\mathrm{fact,cum}) = 41.4$,
$W(\mathrm{ts,cum}) = 125$ kJ

Gibbs energy increments:

$$\mathrm{DQF(fact)} = 38.1 \text{ kJ};$$
$$\mathrm{G(fact)} = \mathrm{G(tr)} + \frac{5}{7}\mathrm{G(gru)} - \frac{5}{7}\mathrm{G(cum)} + \mathrm{DQF(fact)}$$
$$\mathrm{DQF(cumm)} = -22.2 \text{ kJ}$$

Hornblende (Hbl): $(Ca,Mg)_2^{M4}(Fe,Mg)_3^{M13}(Fe,Mg,Al)_2^{M2}$ $(Al,Si)_2^{T1}Si_6O_{22}(OH)_2$

Mineral end-members:

$$\text{Tremolite (tr)} : Ca_2Mg_5Si_8O_{22}(OH)_2$$

$$\text{Ferroactinolite (fact)} : Ca_2Fe_5Si_8O_{22}(OH)_2$$

$$\text{Tschermakite (ts)} : Ca_2Mg_3Al_2Al_2Si_2O_{22}(OH)_2$$

$$\text{Cummingtonite (cum)} : Mg_7Si_8O_{22}(OH)_2$$

Compositional variables:

$x(\mathrm{Hbl}) = \mathrm{Fe}/(\mathrm{Fe} + \mathrm{Mg})$ $y(\mathrm{Hbl}) = X\mathrm{Al,M2}$ $\mathrm{ca(Hbl)} = X\mathrm{Ca,M4}$

Ideal mixing on site activity expressions:

$$x(\mathrm{Ca,M4}) = \mathrm{ca} \quad x(\mathrm{Mg,M4}) = (1-x)(1-\mathrm{ca}) \quad x(\mathrm{Fe,M4}) = x(1-\mathrm{ca})$$

$$x(\mathrm{Mg,M13}) = 1 - x \quad x(\mathrm{Fe,M13}) = x$$

$$x(\mathrm{Mg,M2}) = (1-x)(1-y) \quad x(\mathrm{Fe,M2}) = x(1-y) \quad x(\mathrm{Al,M2}) = y$$

$$x(\mathrm{Al,T1}) = \frac{1}{2}y \quad x(\mathrm{Si,T1}) = 1 - \frac{1}{2}y$$

$$a(\mathrm{tr}) = x(\mathrm{Ca,M4})^2 x(\mathrm{Mg,M13})^3 x(\mathrm{Mg,M2})^2 x(\mathrm{Si,T1})^2$$

$$a(\mathrm{fact}) = x(\mathrm{Ca,M4})^2 x(\mathrm{Fe,M13})^3 x(\mathrm{Fe,M2})^2 x(\mathrm{Si,T1})^2$$

$$a(\mathrm{ts}) = 4x(\mathrm{Ca,M4})^2 x(\mathrm{Mg,M13})^3 x(\mathrm{Al,M2})^2 x(\mathrm{Al,T1}) x(\mathrm{Si,T1})$$

$$a(\mathrm{cum}) = x(\mathrm{Mg,M4})^2 x(\mathrm{Mg,M13})^3 x(\mathrm{Mg,M2})^2 x(\mathrm{Si,T1})^2$$

Regular solution parameters:

$W(\mathrm{tr,fact}) = 9$, $W(\mathrm{tr,ts}) = 20$, $W(\mathrm{tr,cum}) = 45$,
$W(\mathrm{fact,ts}) = 12.9$, $W(\mathrm{fact,cum}) = 41.4$,
$W(\mathrm{ts,cum}) = 125$ kJ

Gibbs energy increments:

$$\mathrm{DQF(fact)} = 38.1\text{kJ};$$
$$\mathrm{G(fact)} = \mathrm{G(tr)} + \frac{5}{7}\mathrm{G(gru)} - \frac{5}{7}\mathrm{G(cum)} + \mathrm{DQF(fact)}$$
$$\mathrm{DQF(cumm)} = -22.2 \text{ kJ}$$

For chlorite activity, composition relations and regular solution parameters were taken from Holland *et al.* (1998), and for garnet, from White *et al.* (2000).